Julia Fleck, Peter Griebel, Adam M. Steinberg, Christoph M. Arndt, Manfred Aigner, Auto-Ignition and Flame Stabilization of Hydrogen / Natural Gas / Nitrogen Jets in a Vitiated Cross-Flow at Elevated Pressure, Int. J. Hydrogen Energy 38(2013), 16441–16452.

The original publication is available at www.elsevier.com

http://dx.doi.org/10.1016/j.ijhydene.2013.09.137

Auto-Ignition and Flame Stabilization of Hydrogen / Natural Gas / Nitrogen Jets in a Vitiated Cross-Flow at Elevated Pressure

Julia M. Fleck[1], Peter Griebel[1](Corresponding author), Adam M. Steinberg[2], Christoph M. Arndt[1], Manfred Aigner[1]

[1]German Aerospace Center (DLR)
Institute of Combustion Technology
Pfaffenwaldring 38-40
70569 Stuttgart, Germany

[2]University of Toronto
Institute for Aerospace Studies
4925 Dufferin Street
Toronto, Canada M3G 5T6

Corresponding Author Contact Information:
Phone: +49 711 6862 381
Fax: +49 711 6862 578
Email: Peter.Griebel@dlr.de

Abstract

The influence of natural gas (NG) on the auto-ignition behavior of hydrogen (H_2)/nitrogen (N_2) fuel jets injected into a vitiated cross-flow was studied at conditions relevant for practical combustion systems (p = 15 bar, $T_{cross\text{-}flow}$ = 1173 K). In addition, the flame stabilization process following auto-ignition was investigated by means of high-speed luminosity and shadowgraph imaging. The experiments were carried out in an optically accessible jet-in-cross-flow (JICF) test section. In a H_2/NG/N_2 fuel mixture, the fraction of H_2 was stepwise increased while keeping the N_2 fraction approximately constant. Two different jet penetration depths, represented by two N_2 fraction levels, were investigated. The results reveal that auto-ignition kernels occurred even for the lowest tested H_2 fuel fraction ($X_{H2/NG} = X_{H2} / (X_{H2} + X_{NG}) = 80\%$), but did not initiate a stable flame in the duct. Increasing $X_{H2/NG}$ decreased the distance between the initial position of the auto-ignition kernels and the fuel injector, finally leading to flame stabilization. The H_2 fraction for which flame stabilization was initiated depended on jet penetration; flame stabilization occurred at lower H_2 fractions for the higher jet penetration depth ($X_{H2/NG}$ = 91% compared to 96%), revealing the influence of different flow fields and mixing characteristics on the flame stabilization process. It is hypothesized that the flame stabilization process is related to kernels extending over the duct height and thus altering the upstream conditions due to considerable heat release. This enabled subsequent kernels to occur close to the fuel injector until they could finally stabilize in the recirculation zone of the jet lee.

Keywords

Auto-ignition, jet in cross-flow, hydrogen, natural gas

Nomenclature

Symbols

B	Vertical blockage ratio
J	Jet to crossflow momentum flux ratio
L	Distance to the fuel injector
p	Pressure
T	Temperature
u	Velocity
X	Mole fraction
$X_{H2/NG}$	Mole ratio of H_2 of the reactive species H_2 and NG in the jet: $X_{H2} / (X_{H2} + X_{NG})$

$X_{N2,high}$ Test case with higher N_2-dilution and jet penetration

$X_{N2,low}$ Test case with lower N_2-dilution and jet penetration

Φ Equivalence ratio

Acronyms

FI Fuel injector

JICF Jet in cross-flow

NG Natural gas

1. Introduction

Utilization of hydrogen (H_2)-rich fuels in modern combustion devices is becoming increasingly relevant due to the need to reduce CO_2 emissions and the demand for alternative energy sources. Hydrogen is a highly reactive molecule with considerably different combustion properties compared to common fuels, such as natural gas (NG). One important characteristic is its high propensity to auto-ignite, which requires careful consideration when designing fuel-flexible low-NO_x combustion technologies such as lean premixed combustion (LPC) systems in stationary gas turbines [1] or H_2-fueled internal combustion engines [2]. Unwanted auto-ignition can lead to severe combustor damage and its avoidance requires detailed understanding of auto-ignition characteristics of H_2-containing fuel blends.

Auto-ignition chemistry is strongly influenced by fuel and oxidizer composition, along with temperature, pressure, and stoichiometry. Typical H_2-rich fuels are syngases derived from the gasification of coal or biomass. Besides inert components like N_2 or carbon dioxide (CO_2), these syngases contain H_2, carbon monoxide (CO) and small amounts of hydrocarbons, predominantly methane (CH_4). While CO was found to significantly influence H_2 auto-ignition chemistry only for relatively high fractions of CO (above 50 vol. %) [3-6], the behavior of H_2/CH_4 systems is more complex. The influence of the H_2/CH_4-ratio on ignition was reported to depend on the temperature and pressure boundary conditions [7-9]. Thiessen et al. [9] modeled the ignition behavior of H_2/CH_4 mixtures for H_2 fractions of 0-100% over a wide range of conditions (T = 800-1500 K, p = 1-100 bar). At lower temperatures, they found that minor fractions of H_2 in CH_4 strongly promote ignition due to enhanced radical production accelerating the rate of methane oxidation. In this temperature range, higher H_2 fractions do not have any further promoting effects. At higher temperatures, where H_2 reactions are dominated by chain-branching reactions, even small fractions of CH_4 act as an ignition inhibitor, since radicals are consumed by CH_4 reactions. The transition between these ranges is pressure dependent. These findings might explain the partially different trends reported in literature. For example, Fotache et al. [10] studied ignition of CH_4 enriched with H_2 in heated air in a non-premixed counterflow flame for pressures between 0.2-8 atm.

They reported that small amounts of H_2 significantly promoted CH_4 ignition, but that the effect decreased with increasing H_2 fraction, and that fractions exceeding 30% did not have any further promoting effect. In contrast, a shocktube study (T = 1132-1553K, $p \approx$ 18-25 atm) of Petersen et al. [11] showed that ignition was more facilitated for the higher tested H_2 fraction: 20% H_2 in CH_4 reduced the ignition delay by a factor of 3, whereas 40% H_2 reduced it by nearly a factor of 10 compared to pure CH_4. This trend is in line with an empirical relation suggested by Cheng and Oppenheim [12] derived from a shocktube study of H_2 in CH_4 varying from 0-100%. Other shocktube studies over such a wide H_2/CH_4-range reported that for H_2 fractions exceeding 80%, ignition is dominated by the H_2 chemistry, exhibiting its complex pressure dependence [13-15]. Nevertheless, both a numerical investigation of Ju and Niioka (T = 1200-1400 K, atmospheric pressure) and a study of Chaumeix et al. (T = 1250-2000 K, p = 1.5-16 bar) showed that even the addition of small amounts of CH_4 to H_2, i.e. less than 15%, drastically decreased the propensity to auto-ignite [16, 17].

The majority of the above mentioned studies were conducted at homogeneous conditions in order to investigate chemical characteristics of auto-ignition. In technical applications, however, auto-ignition is a highly complex process involving turbulent mixing and fluid dynamics, in addition to normal auto-ignition chemistry [18].

The present study aims at investigating the auto-ignition behavior of H_2/N_2 mixtures in the presence of minor amounts of NG, which mainly consists of CH_4, at conditions relevant for technical systems. For this reason, the investigations were carried out in a jet-in-cross-flow (JICF) configuration. JICFs exhibit highly strained regions of non-uniform mixing, reaction rate, and temperature, and therefore mimic conditions of technical relevance [19-21]. In addition to the auto-ignition onset, kernel propagation and the subsequent flame stabilization process was studied using high-speed luminosity and shadowgraph imaging. The chosen operating conditions, namely elevated pressure (15 bar), high cross-flow temperature (1173 K) and velocity (200 m/s), along with $H_2/NG/N_2$ fuel jets being injected into vitiated air, are in the range which is relevant for mixing sections of gas turbine reheat combustors [1, 22-24]. The current work complements recent auto-ignition studies of various H_2/N_2 fuel mixtures [1, 25] in order to provide a better understanding of operating combustion systems, particularly reheat combustors, with H_2-rich fuels.

2. Experiment and Diagnostics

2.1 Combustor Facility

The behavior of $H_2/NG/N_2$ jets in cross-flows was studied in a high-pressure, high-temperature combustion facility. The facility consisted of an air vitiator, a cross-flow channel with fuel injector (JICF test section, see Fig. 1), and a dump combustor. The

JICF test section was comprised of an optically accessible 25 × 25 mm^2 duct with a square cross section, which was arranged downstream of the air vitiator. When inserted into the pressure vessel, the field of view in the test section ranged from about 40 mm upstream of the fuel injector (FI) to 74 mm downstream in the *x*-direction and +/-9 mm in the *y*-direction. The test section windows were convectively air-cooled to prevent thermal damage. The water-cooled metal frame of the duct was coated with a zirconium-oxide thermal barrier coating to minimize heat loss. The total heat loss of the duct was about 6% due to the air and water-cooling systems. Downstream of the optically accessible region, a sudden-expansion geometry allowed the reactive mixture to auto-ignite and to stabilize a flame due to the recirculation zones, after which the exhaust gas left the facility. Further details of the high pressure combustor facility can be found in [1].

2.2 Cross-flow Conditions

For this work, the cross-flow inlet conditions were fixed and the behavior of different jet compositions was studied. The vitiated cross-flow entering the JICF test section was generated using a slightly modified FLOX® combustor [27], which was operated with natural gas at $\Phi \approx 0.43$ and a thermal power of around 430 kW. The exhaust gas was diluted with additional air before entering the test section in order to match a desired oxygen concentration of around 15 vol. %, simultaneously with the desired duct inflow temperature. The total cross-flow mass flow rate was around 550 g/s. The oxygen concentration was monitored through an exhaust gas probe at the duct inlet, 178 mm upstream of the fuel injector, using a gas analyzer (paramagnetism: Magnos 16). The actual FLOX® burner equivalence ratio was calculated from the measured oxygen concentration, from which the total gas composition of the vitiated cross-flow was derived. The mean composition entering the cross-flow duct was X_{O2} = 15.0%, X_{N2} = 76.8%, X_{CO2} = 2.8% and X_{H2O} = 5.4%, with a standard deviation of the measured value of < 0.5%.

During the experiments, the cross-flow conditions were kept constant at a pressure p_{cf} = 15 bar, a set-point temperature T_{cf} = 1173 K, and a bulk velocity u_{cf} = 200 m/s, resulting in a cross-flow Reynolds number of $Re_{cf} = 4 \times 10^5$. The pressure and temperature were measured at a rate of 1 Hz, and from these values and the mass flow rates, the instantaneous cross-flow velocity was calculated. The pressure was measured with a pressure transducer (CerabarS, PMC71) in the inlet of the duct, 195 mm upstream of the fuel injector. The cross-flow temperature was monitored by means of a thermocouple probe (type K) at the axis of symmetry (y = 0 mm), which was permanently installed 110 mm upstream of the fuel injector in the upper duct wall. The probe was shielded with a ceramic casing to minimize radiative heat loss. The boundary conditions of the duct have been measured with respect to vertical temperature profiles, velocity fields, and vitiated air composition in a previous study [1]. These investigations revealed only a slight temperature inhomogeneity over the duct height and a smooth velocity field. Furthermore, exhaust gas measurements have shown extremely low pollutant levels in the cross-flow.

2.3 Fuel Jet Conditions

Fuel jets of various H_2/NG/N_2 mixtures were injected perpendicularly from the lower wall into the vitiated cross-flow through a circular fuel injector orifice with an inner diameter of d_{FI} = 5.6 mm. The fuel jets were at approximately room temperature (between 298 and 318 K, measured in the feed pipe about 40 mm upstream of the fuel injector exit). Two different N_2 mole fractions were studied, namely $X_{N2} \approx$ 55 and 40%, resulting in two different fuel jet velocities (u_{fuel}) and jet penetration depths, as discussed below. These different N_2 mole-fraction cases will be referred to as the $X_{N2,high}$-cases and $X_{N2,low}$-cases, respectively.

The mole ratio of the reactive species (H_2 and NG), which will be described by $X_{H2/NG} = X_{H2} / (X_{H2} + X_{NG})$, was varied according to Table 1. Each value in this table represents a target 'set point' for fuel injection at which measurements were taken. The bold conditions approximately represent the conditions at which flame-stabilizing auto-ignition occurred in the duct. The global equivalence ratio was kept constant at Φ_{glob} = 0.36 for every set point fuel jet mixture, resulting in thermal loads in the range of 440-470 kW. It should be noted, however, that a wide range of different local equivalence ratios were present in the duct during mixing of the jet and the cross-flow [28].

The two different N_2 mole fractions were studied in order to investigate the effects of different jet penetration depths, including different jet/cross-flow mixing rates. The dilution change itself is expected to have a minor influence on the ignition behavior [29]. A crucial parameter for the jet penetration and mixing characteristics of a JICF is the momentum flux ratio J [19, 20, 30]. In the current experiment, J was between 2.8 - 4.3 ($u_{fuel} \approx$ 210 - 260 m/s) for the $X_{N2,high}$ -cases and between 1.2 - 1.9 ($u_{fuel} \approx$ 150 - 200 m/s) for the $X_{N2,low}$ -cases. Based on a correlation of Ref. [30], this corresponds to jet penetration depths of around 11 - 13 mm and 7 - 9 mm, respectively, for the trajectory of maximum jet concentration. This is in line with estimations of the jet penetration from PIV velocity field measurements in the current set-up [1], where it was found that the $X_{N2,high}$ jets crossed the centerline and the $X_{N2,low}$ jets had a slight underpenetration. Complementary to the $X_{N2,high}$- and $X_{N2,low}$-cases, an additional case was conducted to better elucidate the jet penetration effects. In this case, referred to as $X_{N2,low+}$, $X_{H2/NG}$ was kept constant and the N_2-fraction was slowly increased from its $X_{N2} \approx$ 40%-level until a flame stabilized in the duct.

2.4 Test Procedure

The measuring procedure was as follows. Initially, a jet composition of H_2/NG/N_2 was chosen that allowed for steady fuel jet injection without the occurrence of auto-ignition initiating a stable flame in the duct. Starting from this blend, $X_{H2/NG}$ was stepwise increased by substituting H_2 for NG towards the next set point fuel jet composition (cf. Table 1). For each set point composition that did not result in a stable flame in the duct, high-speed videos (described below) were recorded to capture the behavior of possible auto-ignition kernels that did not ignite a stable flame. The procedure was repeated until a H_2-mole fraction was reached at which an auto-ignition event led to flame stabilization in the duct. This will be referred to as the *flame-stabilization limit* in the following. At this point, the high-speed camera was post-triggered and the fuel was shut down to avoid damage to the test section from thermal stresses.

Adjusting to a new jet composition involved three steps. First, the mass flow rate of N_2 was changed to the necessary value for the new mixture. Second, the NG mass flow rate was reduced, which temporary decreased Φ_{glob} since the mass flow rate of the cross-flow was kept constant. Finally, the H_2 mass flow rate was increased to its new set point value. Eight iterations were performed for the $X_{N2,high}$-case and four for the $X_{N2,low}$-case to evaluate the stabilization limits. It is noted that, once the limiting fuel composition was roughly known, the test procedure did not initiate from the lowest H_2 concentration, but from the set point concentration immediately below the stabilization limit.

When flame stabilizing auto-ignition occurred, a rise in both T_{cf} and p_{cf} was observed. This was similar to Ref. [1] and is likely due to the thermal expansion and stronger jet penetration associated with the burning jet that occurred rapidly after the onset of auto-ignition [31], as will also be discussed in section 3.4. As in Ref. [1], the conditions in the duct prior to flame stabilization were defined by the values of T_{cf} and p_{cf} immediately prior to the rise in both quantities. In cases of non-stabilizing auto-ignition events at steady state jet conditions, the T_{cf} and p_{cf} values presented are averaged over one minute.

For different fuel jet compositions, the so-derived instantaneous cross-flow temperature immediately prior to the stabilizing auto-ignition events differed from the target value (1173 K) value by a maximum of 2%. This deviation was due to the day-to-day-reproducibility and the operational standard deviation at steady-state conditions, both of which were in the range of 1%. The difference of the instantaneous pressure from the design value corresponded to the standard deviation of up to 1%.

2.5 High-Speed Imaging - Luminosity

In order to visualize the auto-ignition events in the duct, the broadband flame luminosity was recorded with a high-speed camera (LaVision HSS6, an HSS5 was used for two operating points) from the side, detecting light emission in the visible wavelength range (400 - 750 nm). Simultaneous shadowgraph measurements were conducted (described below) during selected test runs. In such cases, the high-speed luminosity camera had to be installed in an angle of 8° due to the additional equipment required for the shadowgraph, which resulted in a negligible bias in the x-direction of 1%. The luminosity camera was equipped with a commercial objective lens (Nikkor), with a focal length of 85 mm and f/1.4 resulting in a projected pixel size of 0.16 mm/pixel. Note that the images were spatially integrated along the line of site of the camera. Images were recorded at frame rates of 20 or 30 kHz, depending on the test run. The camera was operated in the post-triggering mode, wherein images are recorded continuously until a trigger signal is received. In cases with flame stabilization in the duct, the camera was manually triggered immediately after the flame was observed. Images from about 0.7 s (depending on the recording rate and the spatial resolution) before the trigger signal were recorded, allowing the complete development of the auto-ignition induced flame to be captured; typical times from ignition to flame stabilization were in the order of 1 ms. In cases without flame stabilization, the camera was triggered during steady state jet conditions.

2.6 High-Speed Imaging - Shadowgraph

The shadowgraph method was applied to visualize the jet penetrating into the cross-flow, not only during ignition and flame stabilization, but also before flame stabilization, i.e. without a stable flame. An integrating sphere (labsphere USS-800S-005) with a halogen lamp (IHLS-100-005) was used as a light source. A high-speed camera (LaVision HSS 5) equipped with a 100 mm Tokina lens (f/2.8) was installed on the opposite side of the luminosity camera and was triggered simultaneously. The frame rate was 15 kHz, and the field of view covered an axial direction from x = 0 mm to x = 43 mm downstream of the fuel injector instead of capturing the entire visible duct length to increase the spatial resolution. Thus, the sensor resolution of 384 x 384 pixels resulted in 0.12 mm/pixel. The exposure time was 30 µs for most tests, but was reduced to 15 µs for some cases to increase the acuity. Although the exposure time was still not short enough to accurately freeze the quickly moving flow structures, the primary features of the flow field are observable. Image post-processing was applied to remove large-scale, slowly moving structures of the cooling air in the high-pressure-vessel surrounding the duct; instantaneous images were divided by a sliding background image, which was generated from ±10 images around the image of interest.

3. Results and Discussion

3.1 Flame-Stabilization Limits

It was found that jet compositions up to H_2 fractions of $X_{H2,total} \approx 60\%$ (total mean jet composition $X_{H2}/X_{NG}/X_{N2}$ = 60/2/38%) could be achieved before the flame-stabilization limit was reached. This is remarkable since, with pure H_2/N_2 mixtures investigated in previous studies [1, 25] only $X_{H2,total} \approx 25\%$ (total jet composition $X_{H2}/X_{N2} \approx 25/75\%$) could be reached at corresponding cross-flow conditions. In the present experiment, the flame stabilization during transition to a new set point was not always during or after increasing the H_2 fraction (step (3)); in four test runs it occurred while decreasing the NG flow rate (step (2)), even though this temporarily decreased the global equivalence ratio. However, both of these steps increased $X_{H2/NG}$. The results therefore indicate a significant influence of X_{NG} on the auto-ignition behavior, which will be elucidated in the following sections. The repeatability of the flame-stabilization limit was better than 2% standard deviation in fuel composition for different repetitions of each test case (viz. N_2 dilution level). This variation is most likely related to slightly fluctuating inflow boundary conditions, such as temperature fluctuations of the vitiated gas.

For the two jet penetration cases ($X_{N2,high}$, $X_{N2,low}$) different mean ratios of the reactive species ($X_{H2/NG}$) at the flame-stabilization limit were observed. For the high penetration cases the ratio was $X_{H2/NG}$ = 91% (total mean jet composition $X_{H2}/X_{NG}/X_{N2}$ = 40/4/56%), for the low penetration cases it was $X_{H2/NG}$ = 96% (total mean jet composition $X_{H2}/X_{NG}/X_{N2}$ = 60/2/38%). This

difference of 5% is higher than the observed scatter in the repeated runs for the individual test cases. In order to confirm that the difference is related to the influence of jet penetration, an additional experiment was conducted, in which the jet momentum of an $X_{N2,low}$-case was increased by increasing the N_2-dilution, while keeping the ratio of the reactive species $X_{H2/NG}$ constant at 93%. This value was below the mean of flame-stabilization limit of the $X_{N2,low}$-case, but higher than that of the $X_{N2,high}$-case. Increasing the jet penetration through N_2 addition led to flame stabilizing auto-ignition at J = 1.8 ($X_{H2}/X_{NG}/X_{N2} \approx$ 55/4/41%) for both repetitions that were conducted. It can therefore be seen that increasing the jet penetration increases the tendency for flame stabilizing auto-ignition.

In order to elucidate the reasons for these observations, the following sections will address both the auto-ignition characteristics and the dynamics of flame stabilization for the two penetration cases.

3.2 Auto-ignition - Initial Appearance

Images of auto-ignition events were obtained from the high-speed luminosity measurements. These events evolved from localized kernels that were spatially and temporally distributed in the test section, which corresponds to the appearance of auto-ignition for H_2/N_2 mixtures [1, 25, 32]. A kernel is defined as a coherent region exceeding a certain luminosity threshold (background signal + approximately 2 counts).

The high-speed images revealed that auto-ignition kernels occurred not only for H_2 fractions close to the flame stabilization limits, but even for the lowest investigated H_2 fractions (highest NG fractions) of $X_{H2/NG}$ = 80% in the fuel jet. Such kernels convected downstream and left the duct without initiating a stable flame. Therefore they are referred to as *non-stabilizing* kernels. At the flame-stabilization limits, several non-stabilizing kernels could ignite and convect out of the duct before the stable flame was ignited by a particular kernel, the so called *stabilizing* kernel. It was further observed that some kernels occurred without the presence of another kernel in the duct, i.e. no other kernel had formed immediately prior to that particular kernel. These will be referred to as *primary* kernels. Other kernels that ignited while at least one other kernel was present in the duct will be referred to as *secondary* kernels.

The different types of kernels were evaluated with respect to the locations where they initially occurred. The *x*-positions refer to the upstream leading edge of a respective kernel, whereas the *y*-positions are defined using the kernel centroid. Figure 2 shows the spatial distribution of initial kernel locations in the visible region of the duct over the course of a typical $X_{N2,high}$-case at the stabilization limit ($X_{H2/NG}$ = 87%; 8000 images, duration 267 ms). The black symbols represent the non-stabilizing kernels, which were transported out of the duct. They formed prior to the kernel marked in red, which was the stabilizing kernel that initiated a stable flame. The majority of kernels were located in the lower half of the duct, likely because of the low velocity region in the jet wake [1], but kernels also occurred above the centerline. For the $X_{N2,low}$-cases with the lower jet penetration depths, all kernels

were located in the lower half due to the slight under-penetration. Regarding the axial positions, the kernels were distributed over nearly the entire visible length. The stabilizing kernel occurred closest to the fuel injector, which will be discussed below. The wide distribution of initial kernel locations was also found in an auto-ignition study by Markides and Mastorakos [32], and is related to the strong dependence of auto-ignition on the specific histories of fluid parcels with respect to local strain, temperature, and mixture fraction.

3.3. Auto-ignition - Influence of H_2/NG-Ratio

In order to illustrate the influence of minor NG fractions in H_2 on the kernel location, Figure 3 shows the minimum axial distances of primary kernels to the fuel injector (L_{min}) versus $X_{H2/NG}$ for each test case that was captured with the high-speed camera. Only the primary kernels (L_{prim}) were taken into account since locations of secondary kernels might potentially be influenced by primary kernels, as will be discussed below. This means that the position of secondary kernels might not solely be related to the change in $X_{H2/NG}$. However, the stabilizing kernels (L_{stab}) are also plotted (regardless if primary or secondary) in order to visualize the flame-stabilization limits.

In general, Fig. 3 reveals that the kernels tended to occur closer to the fuel injector with increasing H_2 fraction (decreasing NG) in the fuel jet. For both cases the minimum primary kernel distance decreased by approximately 50% between the lowest and highest tested H_2 fractions: They decreased from $L_{min} \approx 55$ mm to $L_{min} \approx 25$ mm for the $X_{N2,high}$-cases and from $L_{min} \approx 45$ mm to $L_{min} \approx 20$ mm for the $X_{N2,low}$-cases, respectively. This confirms that minor NG fractions in the fuel (< 20% in the tested mixtures) significantly influence auto-ignition under the investigated boundary conditions, i.e. increase the ignition delay time which lead to kernels occurring relatively far downstream of the fuel injector. This inhibiting effect is reduced with decreasing NG (increasing H_2) fractions. As a consequence, the ignition delay time decreases, allowing kernels to form closer to the fuel injector. This is in line with the observations reported by Ju and Niioka [16], who numerically investigated H_2/CH_4 and air streams at T = 1200, 1300, and 1400 K in a supersonic mixing layer. Their results showed that, for $X_{H2} > 85\%$, the ignition distance from the location where a reactive mixture was formed drastically decreased with increasing H_2 concentration. Their explanation that small amounts of CH_4 act as a radical sink is in line with that given by Thiessen et al. [9]. According to Thiessen et al., this is characteristic for pressure and temperature conditions where ignition is dominated by chain branching reactions.

Comparing the test cases with high and low penetration ($X_{N2,high}$ and $X_{N2,low}$), a similar primary kernel behavior is observed for ratios of the reactive species in the range of $X_{H2/NG} \leq 95\%$. If at all, the kernels of the $X_{N2,low}$ test cases tended to occur slightly farther upstream (lower L_{min} values), which might be related to the lower dilution level. It is unlikely that mixing is responsible for this behavior since mixing is worse in the $X_{N2,low}$-case and therefore the primary kernels would then be expected to occur farther downstream. This suggests that the differences in flow field and mixing characteristics caused by the different jet momentum flux

ratios are insufficient to substantially change the initial auto-ignition characteristics. Hence, chemical kinetics likely are the dominating mechanism controlling the initial auto-ignition occurrence.

It is noted that, for the $X_{N2,low}$-cases with ratios of the reactive species exceeding $X_{H2/NG} > 95$ %, the values of L_{min} could be relatively high. This is indicative of an increasing propensity to develop stable flames at such high hydrogen fractions; stable flames developed quickly at these conditions regardless of the primary kernel location, as will be further discussed below.

Regarding the flame-stabilization limits, Fig. 3 illustrates that the kernels finally igniting the stable flame occurred considerably closer to the fuel injector than the primary kernels, as mentioned above. Keeping in mind that all stabilizing kernels, with one exception, were secondary kernels, indicates that the secondary kernels might be influenced by primary kernels altering the thermo-fluidic properties within the test section.

In order to verify this observation, the ensemble-mean locations of all secondary and primary kernels were compared for each test case. Figure 4 shows the distances between secondary and primary kernels, $L_{rel} = L_{sec} - L_{prim}$, versus $X_{H2/NG}$. The "$L_{rel} = 0$" -line represents secondary kernels forming at the same axial locations as the primary ones. For $L_{rel} < 0$, the secondary kernels occurred closer to the fuel injector and vice versa.

It can be seen that the majority of secondary kernels occurred upstream of the primary ones. However, this trend was more pronounced for the $X_{N2,high}$-cases than for the $X_{N2,low}$-cases, which will be discussed below. For $X_{H2/NG} < 85\%$, secondary kernels formed at axial positions similar or downstream of the primary ones, or no secondary kernels were detected at all. For $X_{H2/NG} > 85\%$, it is remarkable that the secondary kernels of the $X_{N2,high}$-cases were considerably closer to the fuel injector, while those of the $X_{N2,low}$-cases were approximately at the same positions as the primary kernels. Only when approaching their flame-stabilization limits ($X_{H2/NG} \approx 96\%$) did the secondary kernels of the $X_{N2,low}$-cases shift closer to the fuel injector.

All in all, Fig. 4 reveals that the majority of secondary kernels occurred closer to the fuel injector than primary kernels at corresponding conditions, particularly when approaching the flame-stabilization limits. Thus, it appears that the primary kernels may influence the conditions upstream in the jet region to be more favorable to auto-ignition. Once a kernel occurs close enough to the fuel injector, it can initiate a stable flame. In order to verify this hypothesis, the dynamics of flame stabilization, evaluated from high-speed measurements, will be discussed in the following section.

3.4 Dynamics of Flame Stabilization

Instantaneous high-speed luminosity and shadowgraph images were used to elucidate the flame stabilization process. Figure 5 shows typical luminosity images from a $X_{N2,high}$ test run at $X_{H2/NG} = 93\%$ (its flame stabilization limit). Representative images were chosen that cover the temporal evolution beginning with the primary kernel, which was defined to occur at $t = 0$ ms, until the flame stabilized at the fuel jet injector. The intensity scaling was chosen to display the first occurrence of auto-ignition

kernels, so that further developed kernels of higher intensity are beyond the saturation limit of the color map. The primary kernel was first detected at x = 35 mm (upstream leading edge) in the lower half of the duct (image no. 1). It is noted that the lower margin of the field of view, where the kernel occurred, is still approximately 3 mm above the lower duct wall. After the first occurrence, the kernel increased in size and intensity while propagating downstream and finally spreading over the entire visible duct height (images no. 2-4). At this state, non-stabilizing secondary kernels (circled in yellow) occurred upstream of the flame region (images no. 5, 7). These kernels also increased in size, propagated downstream and merged with the flame region. After approximately t = 0.7 ms (image no. 11), a stabilizing secondary kernel formed close to the fuel injector (x = 15 mm). Unlike the other kernels, this kernel's upstream leading edge propagated towards the fuel injector, while the downstream portion merged with the flame region that had originally emerged from the primary kernel. Thus, a stable flame at the fuel injector had developed within approximately 0.9 ms.

These observations suggest that flame stabilization is related to kernels spreading over the entire duct height downstream of the injector, thereby altering the conditions upstream through the considerable volumetric expansion. Previous studies have shown that a reacting jet penetrates deeper into the cross-flow than a non-reacting jet [31, 33], which was related to the buoyancy and volumetric expansion of the reaction zone lifting the jet body.

To study the influence of a downstream flame region on the upstream conditions, the high-repetition-rate shadowgraph images were used to investigate the jet and mixing behavior. Figure 6 displays mean shadowgraphs of the test run shown in Fig. 5 ($X_{H2/NG}$ = 93%), with Figs. 6a and b representing the non-reacting and reacting jet (after the flame stabilizing auto-ignition event), respectively. The jet's core is visible as a coherent low intensity region close to the fuel injector (x = 0 mm). Unfortunately, the detailed jet trajectory cannot be directly evaluated from these images due to the rapid mixing of jet and cross-flow fluid resulting in a rapidly decaying signal. However, a parameter describing the alteration in jet penetration can be determined from the inclination angle α at the upstream edge of the jet. This angle was obtained from a line fitted to the lowest visible 5 mm of the low intensity region (sloped dashed line before flame stabilization, solid line after flame stabilization). During the flame stabilization process, α increased from $\alpha \approx 42°$ to $\alpha \approx 54°$, indicating a higher jet penetration after the flame is stabilized in the duct. As a consequence, this changed jet penetration will also lead to different flow and mixing characteristics.

For the auto-ignition and flame stabilization processes investigated here, the exact moment when the jet inclination angle begins to increase is of particular interest, as it is an indicator for the moment when the upstream conditions begin to change. This process can be investigated using the high-repetition-rate shadowgraph images, which were obtained simultaneously with every second luminosity image. Figure 7a displays the instantaneous shadowgraph images corresponding to luminosity images shown in Fig. 5. Since the frame rate in the shadowgraph imaging was half the frame rate of the luminosity images, representative images at slightly different time intervals are shown. Figure 7b shows shadowgraphs of a particular test run, in which the flame

stabilizing kernel was a primary kernel. This run was also an $X_{N2,high}$-case ($X_{H2/NG}$ = 92%). Similar to the luminosity series (Fig. 5), the sequences show images from the occurrence of the primary kernel until formation of a stable flame. Each image is overlaid with contours of flame regions taken from the simultaneously captured luminosity image (green line). Additionally, lines visualizing the mean jet inclination angles of the non-reacting (sloped dashed white line) and the reacting (sloped solid white line) jets are plotted, which were derived from mean images of the respective test runs as described above. It is noted that the spatial and temporal resolution of the shadowgraph imaging was not high enough to resolve the smallest turbulent structures of this highly turbulent flow. Nevertheless, the incoming cross-flow and the penetrating fuel jet are clearly distinguishable by their different flow patterns, as marked by the second order density variation. The undisturbed cross-flow from the left is characterized by small-scale, mainly horizontal structures of the highly turbulent flow. In contrast, the jet penetrating from the fuel injector is characterized by comparably large-scale, distinct, coherent structures in the near field. These structures decay further downstream, around $x \approx 20$ mm, indicating the mixing of the fuel jet and the cross-flow.

Considering the image sequence in Fig. 7a, the instantaneous jet inclination at $t = 0$ ms (when the primary kernel ignited) agreed well with that of the mean image from the non-reacting flow; the upper jet boundary just crossed the duct centerline. This penetration behavior was sustained while the kernel increased in size and convected downstream (images no. 2 - 4). However, in image no. 4, a significant change is apparent in the jet flow pattern; structures in the jet wake became more disorganized and there was a bulk change in the jet trajectory. This indicates an influence of the, now large, flame region on the conditions upstream. This flow pattern persisted in the next image (no. 5), wherein a non-stabilizing secondary kernel occurred. Subsequently, the jet penetration depth gradually increased, until its large-scale structures nearly reached the upper border of the visible region (images no. 6-10). At this point, the jet inclination angle had increased to that of the reacting jet mean, which is visualized by the solid line (cf. Fig. 6b). The flame stabilizing kernel formed in the next image, close to the fuel injector in the jet lee, and the flame propagated upstream and stabilized due to the recirculation zone in the jet lee [21].

Figure 7b shows the only test run in which a primary kernel resulted in flame stabilization. The image of the first kernel occurrence in the luminosity images was not exactly captured with shadowgraph imaging. Therefore, the images immediately prior to (image no. 1) and after (image no. 2) the first occurrence are shown. Immediately after formation, the kernel's upstream leading edge remained at roughly the same axial position, while it increased in size and expanded in the downstream direction (images no. 2, 3). This is different to the primary kernel in Figs. 5 and 7a, which immediately convected downstream. A possible explanation for this behavior is that this kernel was the primary kernel forming closest to the fuel injector of all $X_{N2,high}$-cases (x = 24 mm). In this region, the axial velocity is significantly lower than the bulk value because of the jet wake [1]. The flame speed therefore was probably high enough to balance the axial velocity and the kernel kept its axial position. After the kernel had spread over the entire duct height, the structure in the jet wake region upstream of the kernel altered, similar to Fig. 7a (image no. 4),

indicating a changing flow pattern. Like in Fig. 7a, the jet was then gradually lifted (images no. 4-7), and the upstream leading edge of the flame began to propagate upstream until it stabilized at the fuel jet injector.

In both test runs shown in Fig. 7, the shadowgraphs clearly reveal that the jet was lifted before the flame stabilized at the fuel injector; lifting of the jet appears to be a cause of the final flame stabilization rather than a consequence. The alteration of upstream conditions likely originates from the flame region expanding over the entire duct height, which leads to increased heat release. It is known that heat addition in a flow can strongly influence conditions and that the impact depends on the amount of heat release [34].

The physical processes changing the upstream conditions during ignition can be approximated by considering the system as a constant area duct with heat addition, which is the classical Rayleigh flow. This yields an order of magnitude approximation of the property changes between the reacting and non-reacting flows [34]. The jet is considered as a heat source only, neglecting jet mass, y-momentum, and enthalpy flux. The heat release in the duct changes the conditions upstream of the reaction zone (C1) into the downstream conditions (C2). Prior to flame stabilization, conditions C1 are considered to be the set-point duct inlet conditions ($p_{cf,1}$ = 15 bar, $T_{cf,1}$ = 1173 K), which result in a Mach-number of $M_{cf,1}$ = 0.29. It is noted that, in reality, these conditions may vary according to the standard deviation (see section 2.4). The cross-flow is considered as a calorically perfect gas with constant specific heat (which is not an accurate assumption in this temperature range, but is sufficient for the current estimation). The mean jet composition at ignition for the $X_{N2,high}$-case ($X_{H2}/X_{NG}/X_{N2}$ = 40/4/56%) is used for the estimation, which for Φ_{glob} = 0.36 results in the heat added per unit mass of q = 705 kJ/kg assuming complete combustion. With these assumptions, the Raleigh flow equations yield a pressure loss due to heat addition of $dp_{1,2}$ = 1.3 bar, and a downstream temperature of $T_{cf,2}$ = 1850 K, which results in $M_{cf,2}$ = 0.4. Since shortly after ignition the existing pressure boundary conditions downstream of the flame can be considered as approximately constant in the current setup, the increase in pressure drop due to heat release requires a pressure increase at the inlet of the duct of $dp_{1,2}$. Assuming adiabatic compression, this also yields an increase in the upstream temperature $T_{cf,1}$ of $dT \approx$ 30 K and an inlet velocity decrease by $du_{cf,1} \approx$ 13 m/s. The temperature rise is in good agreement with the measurements at the duct inlet, which showed a temperature peak of $T_{cf,1}$, comparing the state prior to and after ignition, of approximately $dT \approx$ 20-40 K, depending on the test run. The measured pressure rise was $dp \approx$ 0.3-0.5 bar. The pressure level, however, increased more slowly than the temperature and usually did not reach the peak value before the fuel was shut down.

Based on this analysis, it is probable that the rise in upstream pressure and temperature become increasingly significant for a higher heat release. As soon as a flame kernel extends over the entire duct height, the entire cross-flow is affected by the heat release and no cold streaks can pass the heat release zone. The higher inlet temperature likely reduces the ignition delay and increases the flame speed. Furthermore, the flow is decelerated, as shown earlier, and might temporary be slowed down even further during the unsteady process of ignition creating the sudden pressure loss over the duct. In addition, the lifting jet might

increase the extent of the low velocity region in the jet wake, and particularly that of the recirculation zone in the jet lee, which depends on the jet penetration depth [21]. This could explain the mentioned change in the flow pattern in the jet wake region appearing in Fig. 7 (images no. 4), and it would increase the residence time of the reactive mixture close to the fuel jet injector. These effects of decreased ignition delay and increased residence time may enable kernels to occur relatively far upstream, to propagate even further upstream through the low velocity region, and eventually to stabilize at the fuel injector. This supports the hypothesis that flame stabilization is related to increasing heat release illustrated by the considerable volumetric expansion of a primary flame kernel spreading over the duct height.

Only exemplary test runs were captured with the shadowgraph imaging as a supplement to the luminosity. Thus, a parameter from the luminosity images was defined to generally validate the hypothesis that flame stabilization was related to the volumetric expansion caused by primary flame kernels. To do so, a vertical blockage ratio B was defined as the vertical extend of the largest flame kernel present in the duct at the moment of secondary kernel formation divided by the height of the viewable region. It is noted that B relates to the flame kernel height within the field of view. However, regarding the recorded images, it is reasonable to expect that kernels with $B = 1$ filled the entire duct in the vertical direction. With respect to the 3rd dimension, it is expected that B also approximately represents a kernel's expansion in the z-direction. This is implied from investigations with pure H_2/N_2 mixtures in the current setup, where a second high-speed camera (top view) provided information about the kernel development in z-direction [1]. The total x-y-area of a kernel was not used for this analysis, as its area could be clipped in the images for kernels that extend downstream of the field of view.

In order to visualize the relationship between the secondary kernels and the vertical blockage ratio B, Fig. 8 shows their axial distances from the fuel injector (L_{sec}) as a function of B. The black line represents the linear fit of the plotted kernels, which comprises all secondary kernels that were detected. The figure illustrates a tendency of secondary kernels to occur closer to the fuel injector with increasing B, as suggested from the above described hypothesis. Interestingly, the behavior is similar for the three different operating conditions (cases $X_{N2,high}$ and $X_{N2,high,}$, along with $X_{N2,low+}$). The relatively strong scatter is related to the wide kernel distribution within a single test run, as explained in section 3.2. All in all, the plot confirms a correlation between secondary kernels and the expansion of flame regions initiated by primary kernels.

Since Fig. 8 implies a distinct relationship between L_{sec} and B, the different stabilization limits for different test cases may be associated with different behaviors of B. It therefore is interesting to further investigate the dependence of B on $X_{N2/NG}$. Figure 9 shows the mean vertical blockage ratio, $B_{mean,}$ at the moment of secondary kernel formation considering all secondary kernels of a respective test run, as a function of $X_{H2/NG.}$ In addition, the vertical blockage ratios for the respective flame stabilizing secondary kernels B_{stab} are shown separately. The plot reveals that B tended to increase for increasing H_2 fractions in the fuel jet. For the lower H_2 fractions of $X_{N2/NG} < 85\%$, small values of $B_{mean} \approx 0.2$ were found. At these H_2 fractions, the secondary kernels formed at

similar axial positions as their respective primary kernels (see Fig. 4). B_{mean} considerably increased when approaching the flame-stabilization limit of each case, with maximum values of up to $B_{mean} = 0.8$ for the $X_{N2,high}$-case and $B_{mean} = 0.65$ for the $X_{N2,low}$ -case. This likely was due to the higher reactivity related to the increasing H_2 fraction, which significantly increased the flame speed [35-37] and thus allowed kernels to grow more quickly. In addition, kernels had more time to grow since they occurred increasingly farther upstream, which lead to higher kernel residence times in the duct. The flame-stabilizing kernels occurred at the highest vertical blockage ratios of $B_{stab} > 0.85$, indicating that the largest flame kernel had essentially spread over the entire visible duct height before the stabilizing kernel was generated. This is true even for $X_{H2/NG} \geq 95\%$ in the $X_{N2,low}$-case, where the primary kernels prior to flame stabilization occurred relatively far downstream (see Fig. 3), which led to small values of B_{mean}. The high values of B_{stab} support the hypothesis based on the exemplary flame stabilization process in Figs. 5 and 7, in which the upstream conditions were proposed to be influenced by the heat release zone expanding over the entire duct. This promoted secondary kernels to occur farther upstream and to propagate towards the fuel injector, until they stabilize in the jet wake recirculation zone, anchoring a steady flame.

However, it is noteworthy that not all high blockage ratio kernels ($B > 0.85$) induced a flame stabilizing secondary kernel. This seems reasonable considering the strong dependence of auto-ignition, not only on temperature and pressure, but also on specific histories of fluid parcels with respect to fluid dynamics and mixing (local composition). These are expected to strongly fluctuate, especially in the near field of the jet, where the penetrating fuel jet causes high mixture fraction and velocity gradients [20, 38].

Comparing test case $X_{N2,low}$ with $X_{N2,high}$, it is remarkable that B_{mean} is considerably higher for $X_{N2,high}$ at a given H_2 fraction. In the range of $X_{H2/NG} = 91\%$, i.e. at the mean stabilization limit of $X_{N2,high}$ with $B_{mean} = 0.8$, B_{mean} for the $X_{N2,low}$-case only reaches 0.4. This is probably related to different mixing characteristics of the two cases exhibiting different jet penetration depths. In the $X_{N2,high}$-case, where the fuel jet crossed the duct centerline (see section 2.3), the fuel could spread more quickly over the entire duct height, allowing the kernel to also extend in the upper half. In addition, the auto-ignition kernels initially could form at higher vertical positions, which allowed them to extend in all directions. In contrast, kernels in the $X_{N2,low}$-case generally formed closer to the lower wall, which prevented them from extending downwards. The lower vertical blockage ratios for the $X_{N2,low}$-cases likely allowed cold streaks of the cross-flow to pass the heat release region, which may reduce the impact of such a flame region on the upstream conditions.

Assuming that flame stabilization in the duct is greatly related to increased heat release illustrated by high vertical blockage ratios could therefore explain why the stabilizing limit for the $X_{N2,high}$-cases was at lower $X_{H2/NG}$ compared to the $X_{N2,low}$-cases: These cases exhibited a higher jet penetration depth leading to high vertical blockage ratios, allowing for earlier flame stabilization. This would lead to the conclusion that, while the initial occurrence of auto-ignition kernels is not significantly changed by the different

jet penetration characteristics (see section 3.2), the development of kernels into a stable flame at the fuel injector depends strongly on the jet fluid dynamics and mixing.

4. Summary and Conclusions

The impact of minor amounts of natural gas on auto-ignition of hydrogen/nitrogen jets injected into a vitiated cross-flow has been experimentally investigated at engine relevant conditions (T = 1173 K, p = 15 bar). In addition, the dynamics of the flame stabilization process following auto-ignition were elucidated using high-speed luminosity and shadowgraph imaging. Two different ranges of jet momentum flux ratios (J = 1.2 - 1.9 and 2.8 - 4.3) have been studied by using different N_2 dilution levels ($X_{N2} \approx$ 40% and 55%, respectively). While keeping N_2 approximately constant at one of the two levels, the H_2 mole ratio in the reactive species, $X_{H2/NG} = X_{H2} / (X_{H2} + X_{NG})$, was increased until auto-ignition initiated stable combustion in the duct. The main conclusions of this study are the following:

- Small amounts of NG in the fuel jet significantly influenced the auto-ignition and flame stabilization behavior under the investigated conditions. NG inhibited auto-ignition, allowing the use of $X_{H2,total}$ = 60% (total mean jet composition $X_{H2}/X_{NG}/X_{N2}$ = 60/2/38%) before the flame-stabilization limit was reached, compared to $X_{H2,total} \approx$ 25% with pure H_2/N_2 mixtures investigated at corresponding conditions in previous studies [1, 25].
- Besides auto-ignition kernels that initiate stable combustion in the duct, kernels were observed that did not lead to flame stabilization, but convected out of the duct. Those kernels occurred even for the lowest H_2 fuel fraction.
- Increasing $X_{H2/NG}$ in the fuel jet decreased the ignition delay time, leading to kernels occurring closer to the fuel injector for both investigated N_2 dilution levels.
- The flame stabilization process was related to kernels extending over the duct height, which altered the upstream conditions due to considerable heat release. This enabled subsequent kernels to occur close to the fuel injector and to travel upstream through the low velocity region until they finally stabilized a flame in the recirculation zone of the jet lee.
- The flame stabilization process was significantly influenced by fluid dynamics and mixing, leading to different mean stabilization limits for the two different jet penetration depths ($\overline{X}_{H2/NG} = 91$ and 96%, respectively), whereas initial auto-ignition did not seem to be significantly changed by the different jet penetration characteristics studied.

Acknowledgements

The authors would like to thank the test rig staff Uwe Prestel, Dominik Lebküchner, Karl-Heinz Ferst and Steffen Peukert for their technical support during the measurements.

References

[1] Fleck J, Griebel P, Steinberg AM, Stöhr M, Aigner M, Ciani A. Autoignition limits of hydrogen at relevant reheat combustor operating conditions. J Eng Gas Turbines Power 2012;134(4):041502-1-8.

[2] Gomes Antunes JM, Mikalsen R, Roskilly AP. An experimental study of a direct injection compression ignition hydrogen engine. Int J Hydrogen Energy 2009;34:6516-22.

[3] Herzler J, Naumann C. Shock tube study of the ignition of lean CO/H_2 fuel blends at intermediate temperatures and high pressure. Combust Sci Tech 2008;180:2015-28.

[4] Kalitan DM, Petersen EL, Mertens JD, Crofton MW. Ignition of lean CO/H_2/air mixtures at elevated pressures. ASME 2006; GT2006-90488.

[5] Mittal G, Sung CJ, Fairweather M, Tomlin AS, Griffiths JF, Hughes KJ. Significance of the HO_2+CO reaction during the combustion of $CO+H_2$ mixtures at high pressures. Proc Combust Inst 2007;31:419-27.

[6] Keromnes A, Metcalfe WK, Heufer KA, Donohoe N, Das AK, Sung C et al. An experimental and detailed chemical kinetic modeling study of hydrogen and syngas mixture oxidation at elevated pressures. Combust. Flame 2013;160:995-1011.

[7] Gersen S, Anikin NB, Mokhov AV, Levinsky HB. Ignition properties of methane/hydrogen mixtures in a rapid compression machine. Int J Hydrogen Energy 2008;33:1957-64.

[8] Huang J, Bushe WK, Hill PG, Munshi SR. Experimental and kinetic study of shock initiated ignition in homogeneous methane-hydrogen-air mixtures at engine-relevant conditions. Int J Chem Kinet 2006;38:221-33.

[9] Thiessen S, Khalil E, Karim G. The autoignition in air of some binary fuel mixtures containing hydrogen. Int J Hydrogen Energy 2010;35:10013-17.

[10] Fotache CG, Kreutz TG, Law CK. Ignition of hydrogen-enriched methane by heated air. Combust Flame 1997;110(4):429-40.

[11] Petersen EL, Hall JM, Smith SD, de Vries J, Amadio A, Crofton MW. Ignition of lean methane-based fuel blends at gas turbine pressures. J Eng Gas Turbines Power 2007;129 GT2005-68517:937-44.

[12] Cheng RK, Oppenheim AK. Autoignition of methane-hydrogen mixtures. Combust Flame 1984;58:125-39.

[13] Herzler J, Naumann C. Shock-tube study of the ignition of methane/ethane/hydrogen mixtures with hydrogen contents from 0% to 100% at different pressures. Proc Combust Inst 2009;32(1):213-20.

[14] Zhang Y, Huang Z, Wei L, Zhang J, Law CK. Experimental and modeling study on ignition delays of lean mixtures of methane, hydrogen, oxygen, and argon at elevated pressures. Combust Flame 2012;159(3):918-31.

[15] Zhang Y, Jiang X, Wei L, Zhang J, Tang C, Huang Z. Experimental and modeling study on auto-ignition characteristics of methane/hydrogen blends under engine relevant pressure. Int J Hydrogen Energy 2012;37:19168-76.

[16] Ju Y, Niioka T. Ignition simulation of methane/hydrogen mixtures in a supersonic mixing layer. Combust Flame 1995;102:462-70.

[17] Chaumeix N, Pichon S, Lafosse F, Paillard C. Role of chemical kinetics on the detonation properties of hydrogen/natural gas/air mixtures. Int J Hydrogen Energy 2007;32:2216-26.

[18] Mastorakos E. Ignition of turbulent non-premixed flames. Prog Energy Combust Sci 2009;35:57-97.

[19] Karagozian AR. Transverse jets and their control. Prog Energy Combust Sci 2010;36:531-53.

[20] Smith SH, Mungal MG. Mixing, structure and scaling of the jet in crossflow. J. Fluid Mech. 1998;357:83-122.

[21] Steinberg AM, Sadanandan R, Dem C, Kutne P, Meier W. Stabilization mechanisms of hydrogen jet flames in cross-flows. Proc Combust Inst 2013;34:1499-507.

[22] Joos F, Brunner P, Schulte-Werning B, Syed K, Eroglu A. Development of the sequential combustion system for the ABB GT24/GT26 gas turbine family. ASME 1996;1996-GT-315.

[23] Güthe F, Hellat J, Flohr P. The reheat concept: The proven pathway to ultralow Emissions and high efficiency and flexibility. J Eng Gas Turbines Power 2009;131:021503 1-7.

[24] Weydahl T, Poyyapakkam M, Seljeskog M, Haugen NEL. Assessment of existing H_2/O_2 chemical reaction mechanisms at reheat gas turbine conditions. Int J Hydrogen Energy 2011;36:12025-34.

[25] Fleck JM, Griebel P, Steinberg AM, Arndt CM, Naumann C, Aigner M. Autoignition of hydrogen/nitrogen jets in vitiated air crossflows at different pressures. Proc Combust Inst 2012;34(2):3185-92.

[26] Fleck JM, Griebel P, Steinberg AM, Stöhr M, Aigner M, Ciani A. Experimental investigation of a generic, fuel flexible reheat combustor at gas turbine relevant operating conditions. ASME 2010;GT2010-22722.

[27] Lückerath R, Meier W, Aigner M. FLOX® Combustion at high pressure with different fuel compositions. J Eng Gas Turbines Power 2008;130:011505 1-7.

[28] Sadanandan R, Fleck J, Meier W, Naumann C. 2D mixture fraction measurements in a high pressure and high temperature combustion system using NO tracer-LIF. Appl. Phys. B, 2012;106:185-96. [29] Blouch JD, Law CK. Effects of turbulence on nonpremixed ignition of hydrogen in heated counterflow. Combust Flame 2003;132:512-22.

[30] Lefebvre AH; Gas turbine combustion. Washington: Hemisphere; 1983.

[31] Mörtberg M, Blasiak W, Gupta AK. Experimental investigation of flow phenomena of a single fuel jet in cross-flow during highly preheated air combustion conditions. J Eng Gas Turbines Power 2007;129:556-64.

[32] Markides CN, Mastorakos E. An experimental study of hydrogen autoignition in a turbulent co-flow of heated air. Proc Combust Inst 2005;30:883-91.

[33] Huang RF, Chang JM. The stability and visualized flame and flow structures of a combusting jet in cross flow. Combust Flame 1994;98(3):267-78.

[34] Anderson JD. Modern compressible flow: With historical perspective. 3rd ed. New York: McGraw-Hill; 2004.

[35] Law CK, Kwon OC. Effects of hydrocarbon substitution on atmospheric hydrogen–air flame propagation. Int J Hydrogen Energy 2004;29:867 – 79.

[36] Di Sarli V, Di BA. Laminar burning velocity of hydrogen–methane/air premixed flames. Int J Hydrogen Energy 2007;32:637 – 46.

[37] Ilbas M, Crayford A, Yilmaz I, Bowen P, Syred N. Laminar-burning velocities of hydrogen–air and hydrogen–methane–air mixtures: An experimental study. Int J Hydrogen Energy 2006;31:1768 – 79.

[38] Rivero A, Ferré JA, Giralt F. Organized motions in a jet in crossflow. J Fluid Mech 2001;444:117-49.

List of figure captions

Fig. 1 JICF test section.

Fig. 2 Spatial distribution of initial ignition kernel locations exemplary for an $X_{N2,high}$-case, $X_{H2/NG}$ = 87%. Black symbols: Kernels convecting out of the duct. Red symbol: Kernel leading to flame stabilization.

Fig. 3 Minimum axial distances between initial auto-ignition kernels and the fuel injector position (L_{min} = 0 mm) over $X_{H2/NG}$.

Fig. 4 Relative axial distances between secondary and primary kernels over $X_{H2/NG}$ for the different test cases. The "L_{rel} = 0"-line marks secondary kernels forming at the same axial locations as their respective primary ones.

Fig. 5 Luminosity images of the flame stabilization process exemplary for an $X_{N2,high}$-case, $X_{H2/NG}$ = 93%. The occurrence of the primary kernel was defined to be t = 0 ms. Occurring secondary kernels are encircled in yellow.

Fig. 6 Mean shadowgraph images of the (a) non-reacting and the (b) reacting fuel jet. The white lines visualize the inclination angle α of the upstream edge of the jet.

Fig. 7 Shadowgraphs of the flame stabilization process, with (a) the test run shown in Fig. 5 and (b) test run with the only primary flame-stabilizing kernel ($X_{N2,high}$-case, $X_{H2/NG}$ = 92%). The green lines mark the contours of flame regions taken from the corresponding luminosity images. The sloped white lines visualize the jet inclination angles of the non-reacting (dashed line) and the reacting (solid line) jets, which were derived from the mean images of the respective test runs.

Fig. 8 Axial distances of initial secondary kernels from the fuel injector (L_{sec} = 0 mm) as a function of the vertical blockage ratio B (maximum vertical extend of the largest flame kernel in the duct at the occurrence of a secondary kernel, divided by the height of the viewable region).

Fig. 9 Vertical blockage ratio B as a function of $X_{H2/NG}$.

Table 1 Investigated target set point fuel concentrations for the $X_{N2,high}$ and $X_{N2,low}$ cases. For every jet composition, also the H_2 fraction in the reactive species $X_{H2/NG}$ is listed. The bold conditions approximately represent the mean compositions at which flame-stabilizing auto-ignition occurred in the duct (flame-stabilization limits).

Case $X_{N2,high}$		**Case $X_{N2,low}$**	
Jet, total	Reactive species	Jet, total	Reactive species
$X_{H2}/X_{NG}/X_{N2}$ [%]	$X_{H2/NG}$ [%]	$X_{H2}/X_{NG}/X_{N2}$ [%]	$X_{H2/NG}$ [%]
34/09/57	80	49/11/40	82.5
36/08/56	82.5	52/09/39	85
37/07/56	85	53/08/39	87.5
39/05/56	89	55/06/39	90
40/04/56	**91**	57/05/38	92.5
		60/02/38	**96**

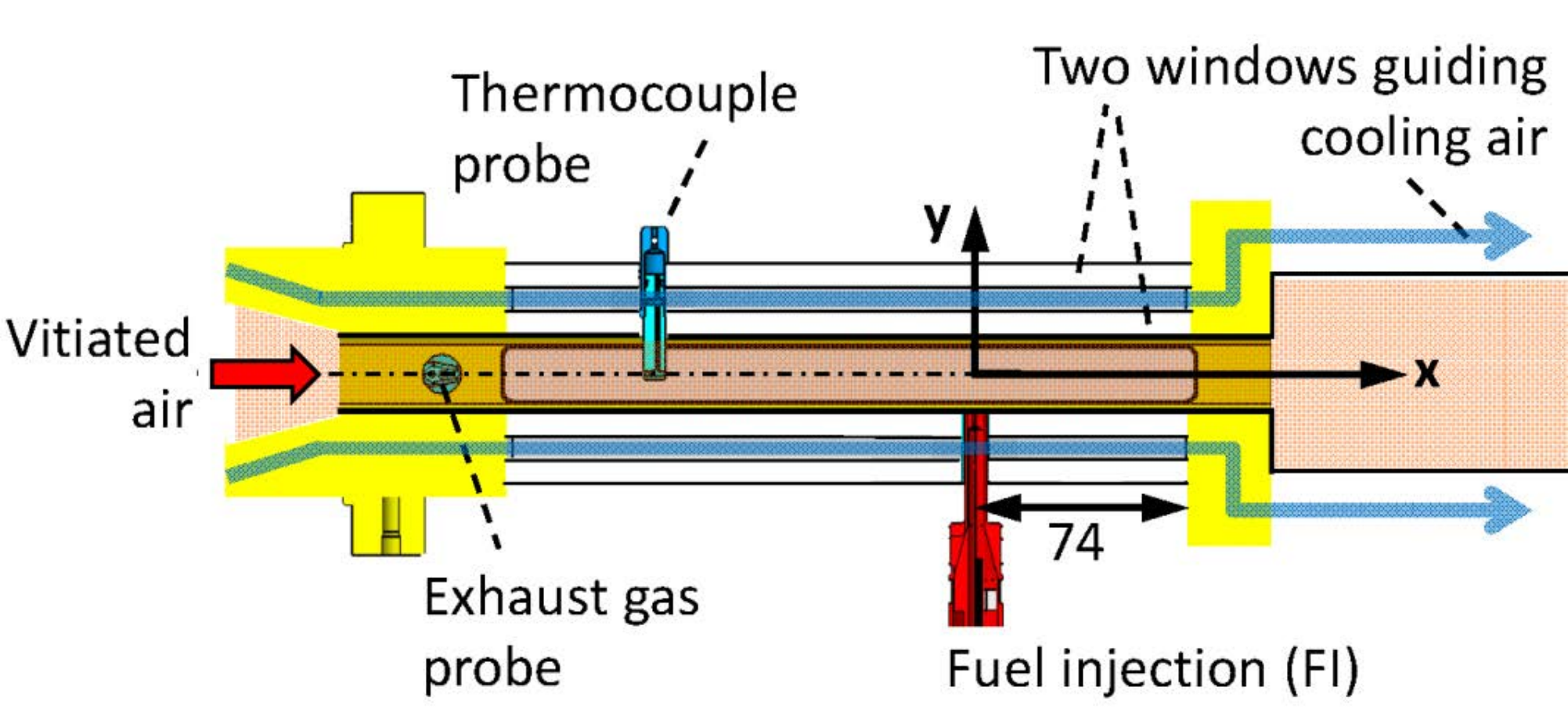
Thermocouple probe
Two windows guiding cooling air
y
Vitiated air
x
74
Exhaust gas probe
Fuel injection (FI)

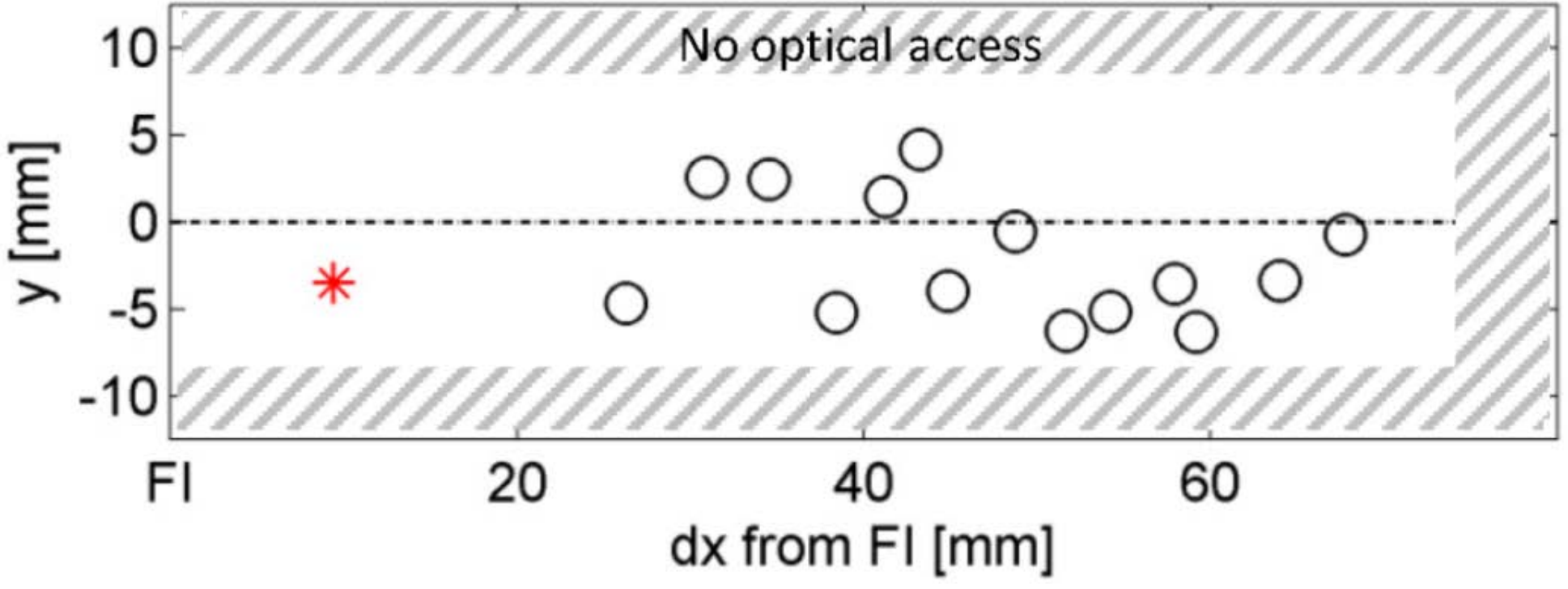
No optical access
10
5
0
-5
-10
y [mm]
FI
20
40
60
dx from FI [mm]

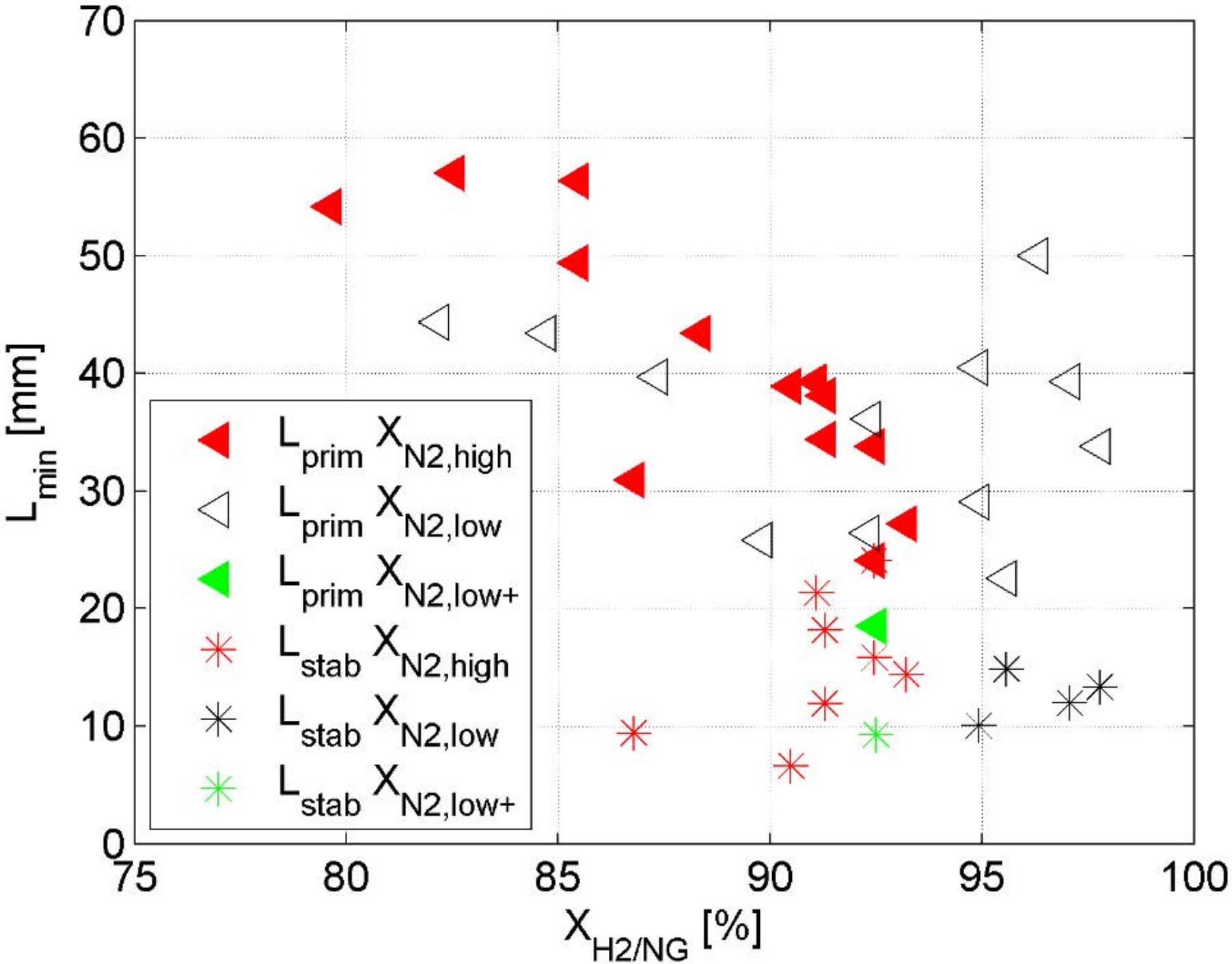
70
60
50
40
30
20
10
0
75
80
85
90
95
100
L_{min} [mm]
$X_{H2/NG}$ [%]
L_{prim} $X_{N2,high}$
L_{prim} $X_{N2,low}$
L_{prim} $X_{N2,low+}$
L_{stab} $X_{N2,high}$
L_{stab} $X_{N2,low}$
L_{stab} $X_{N2,low+}$

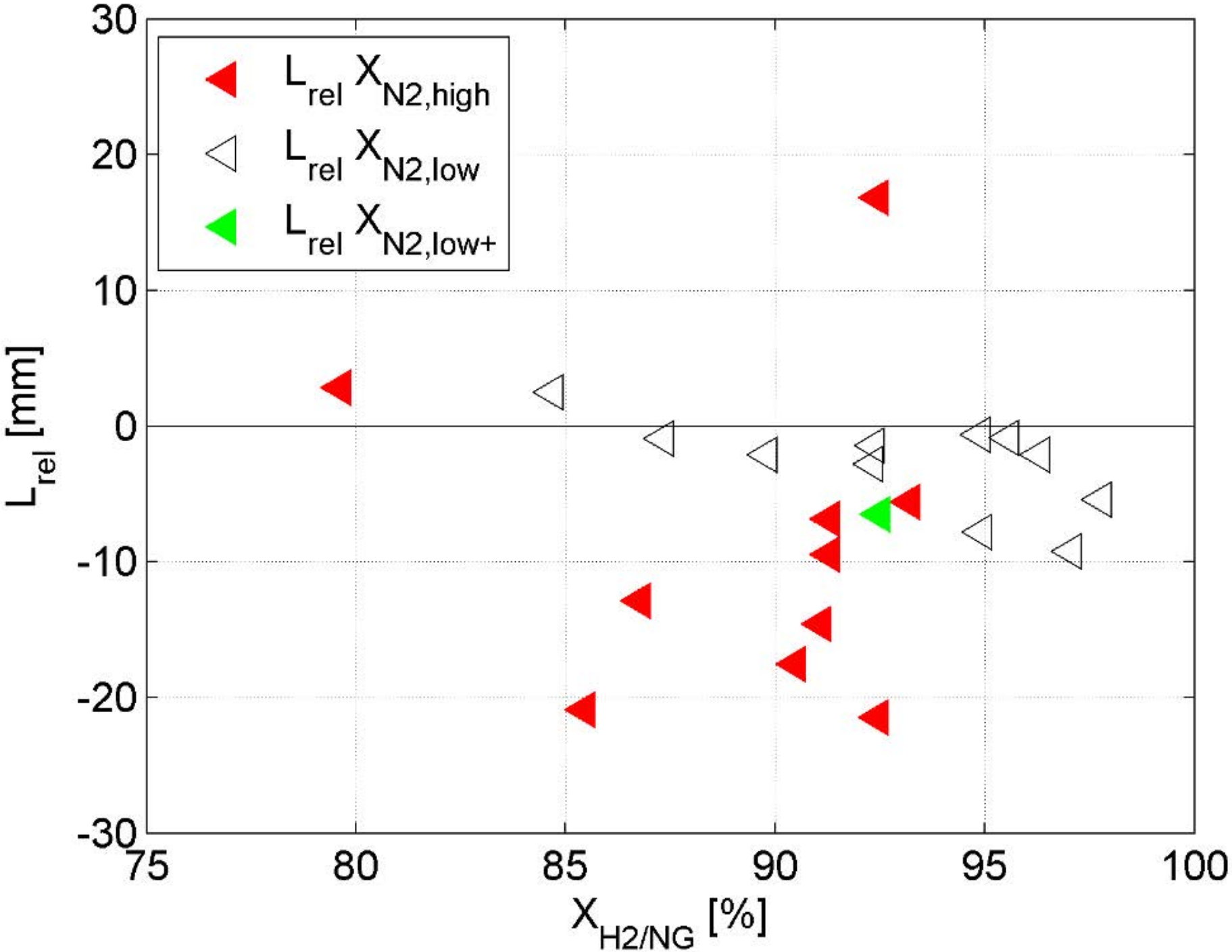
30
20
10
0
-10
-20
-30
75
80
85
90
95
100
L_{rel} [mm]
$X_{H2/NG}$ [%]
L_{rel} $X_{N2,high}$
L_{rel} $X_{N2,low}$
L_{rel} $X_{N2,low+}$

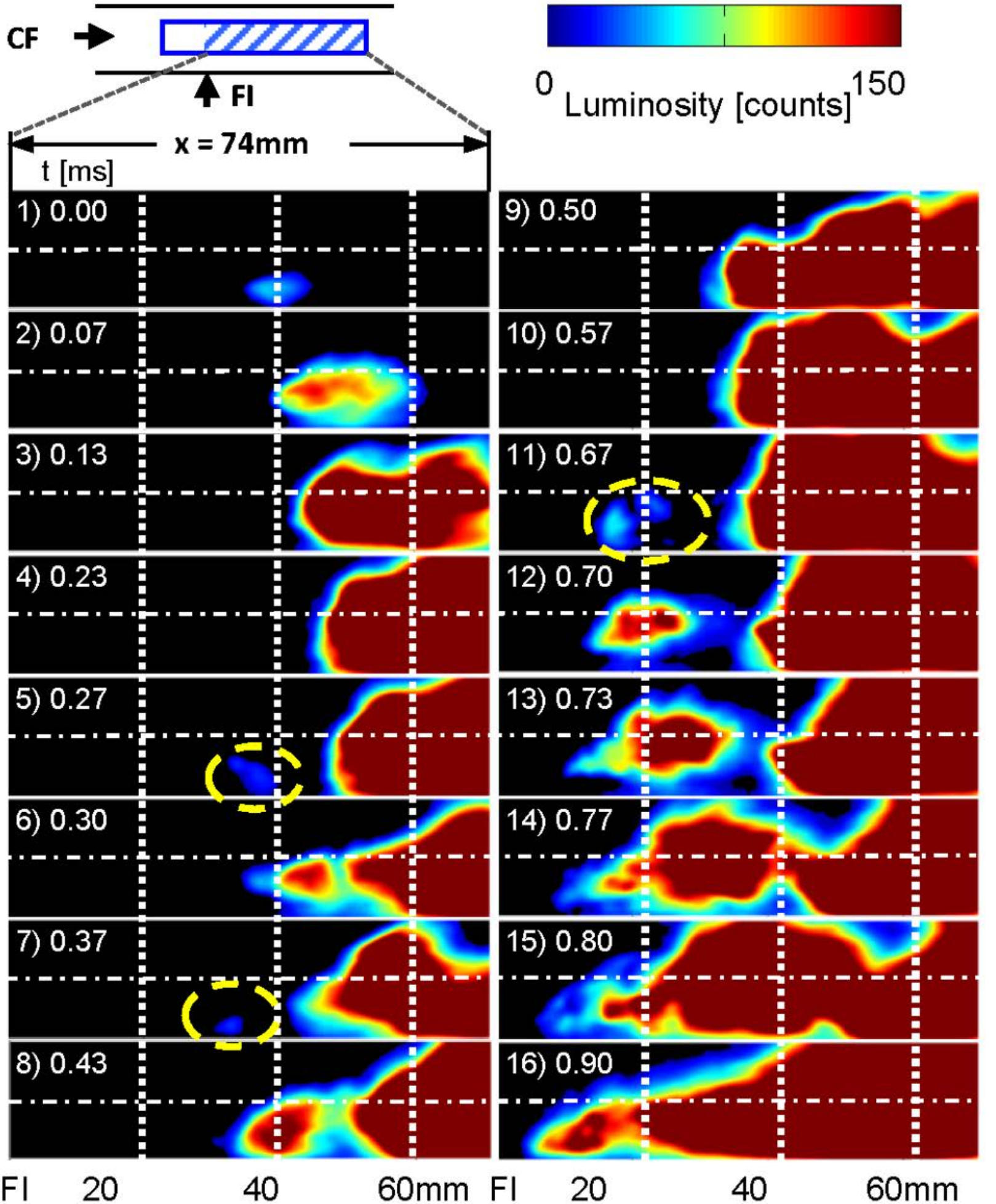
CF
FI
x = 74mm
t [ms]
0
Luminosity [counts]
150
1) 0.00
2) 0.07
3) 0.13
4) 0.23
5) 0.27
6) 0.30
7) 0.37
8) 0.43
9) 0.50
10) 0.57
11) 0.67
12) 0.70
13) 0.73
14) 0.77
15) 0.80
16) 0.90
FI 20 40 60mm
FI 20 40 60mm

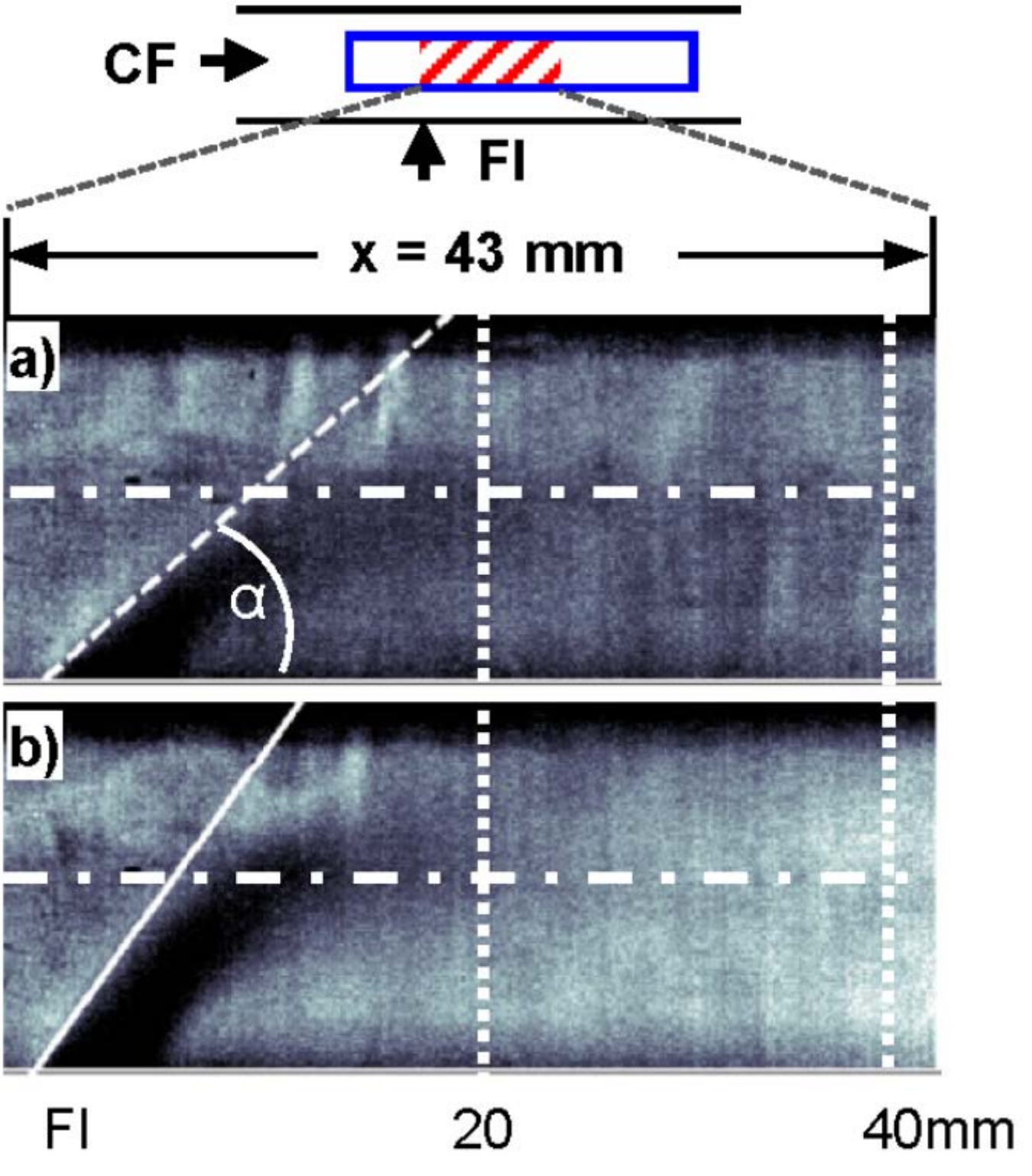
CF
FI
x = 43 mm
a)
α
b)
FI
20
40mm

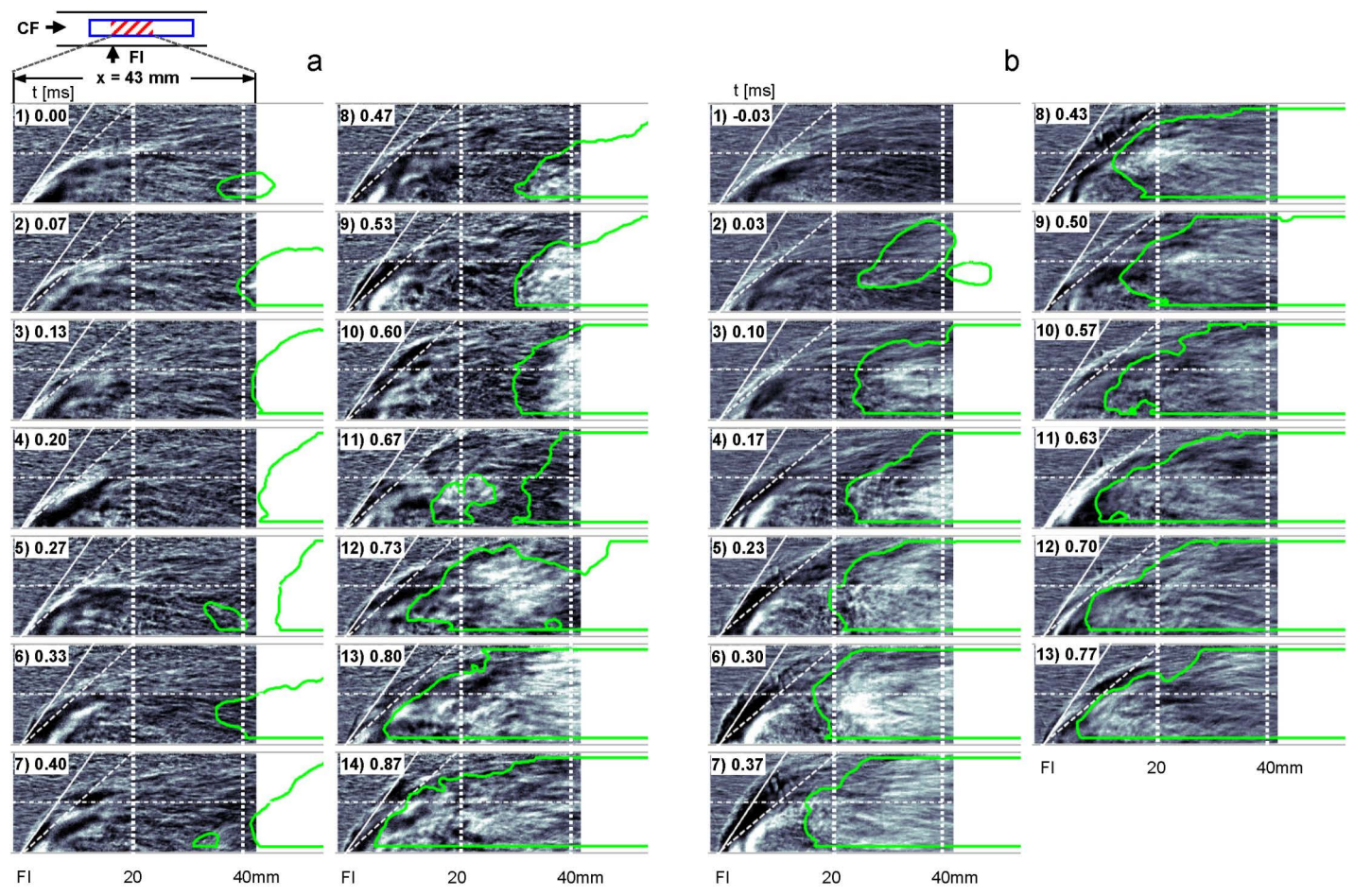
CF
FI
x = 43 mm
t [ms]
a
1) 0.00
2) 0.07
3) 0.13
4) 0.20
5) 0.27
6) 0.33
7) 0.40
8) 0.47
9) 0.53
10) 0.60
11) 0.67
12) 0.73
13) 0.80
14) 0.87
FI
20
40mm
b
t [ms]
1) -0.03
2) 0.03
3) 0.10
4) 0.17
5) 0.23
6) 0.30
7) 0.37
8) 0.43
9) 0.50
10) 0.57
11) 0.63
12) 0.70
13) 0.77
FI
20
40mm

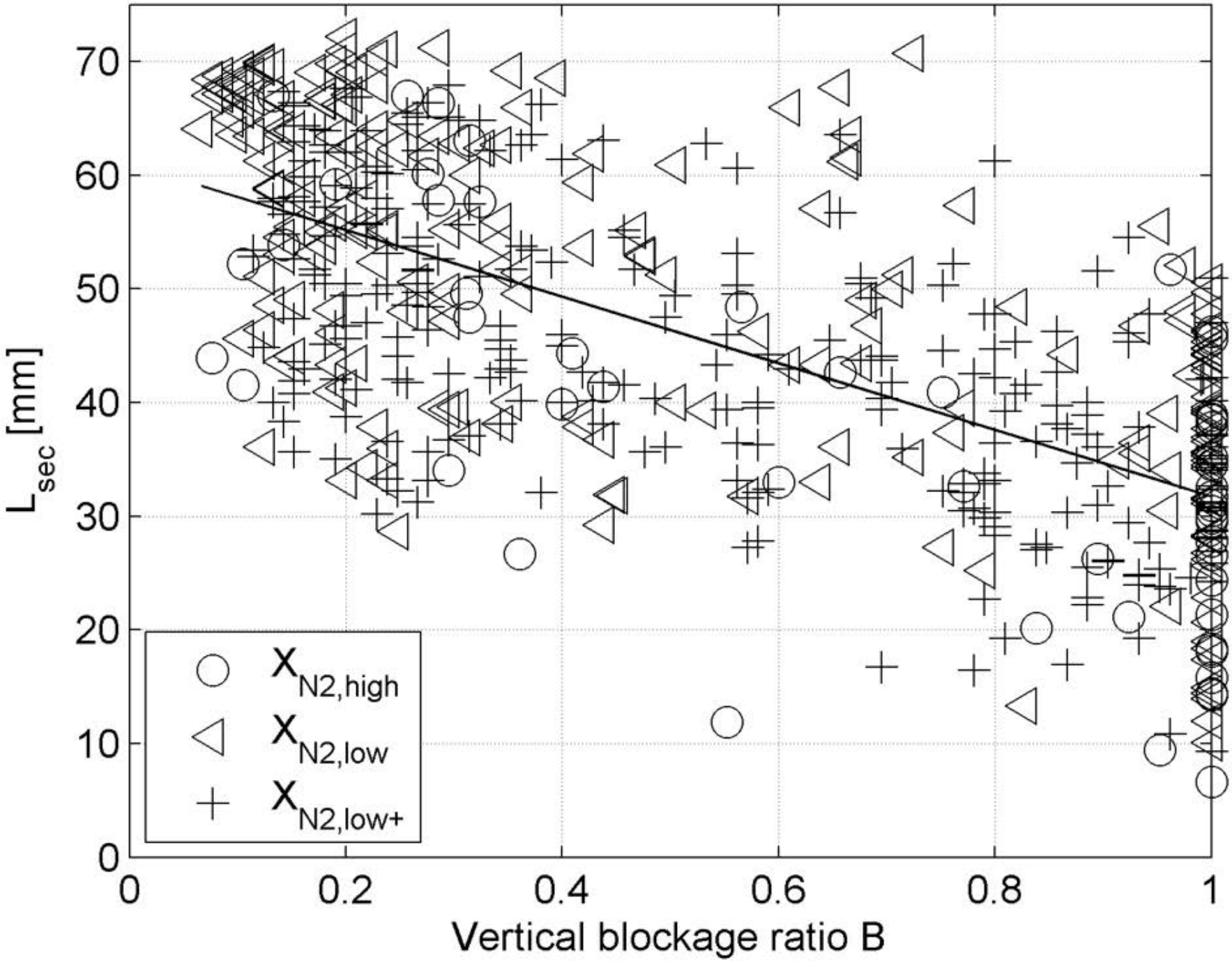
70
60
50
40
30
20
10
0
0
0.2
0.4
0.6
0.8
1
L_{sec} [mm]
Vertical blockage ratio B
$x_{N2,high}$
$x_{N2,low}$
$x_{N2,low+}$

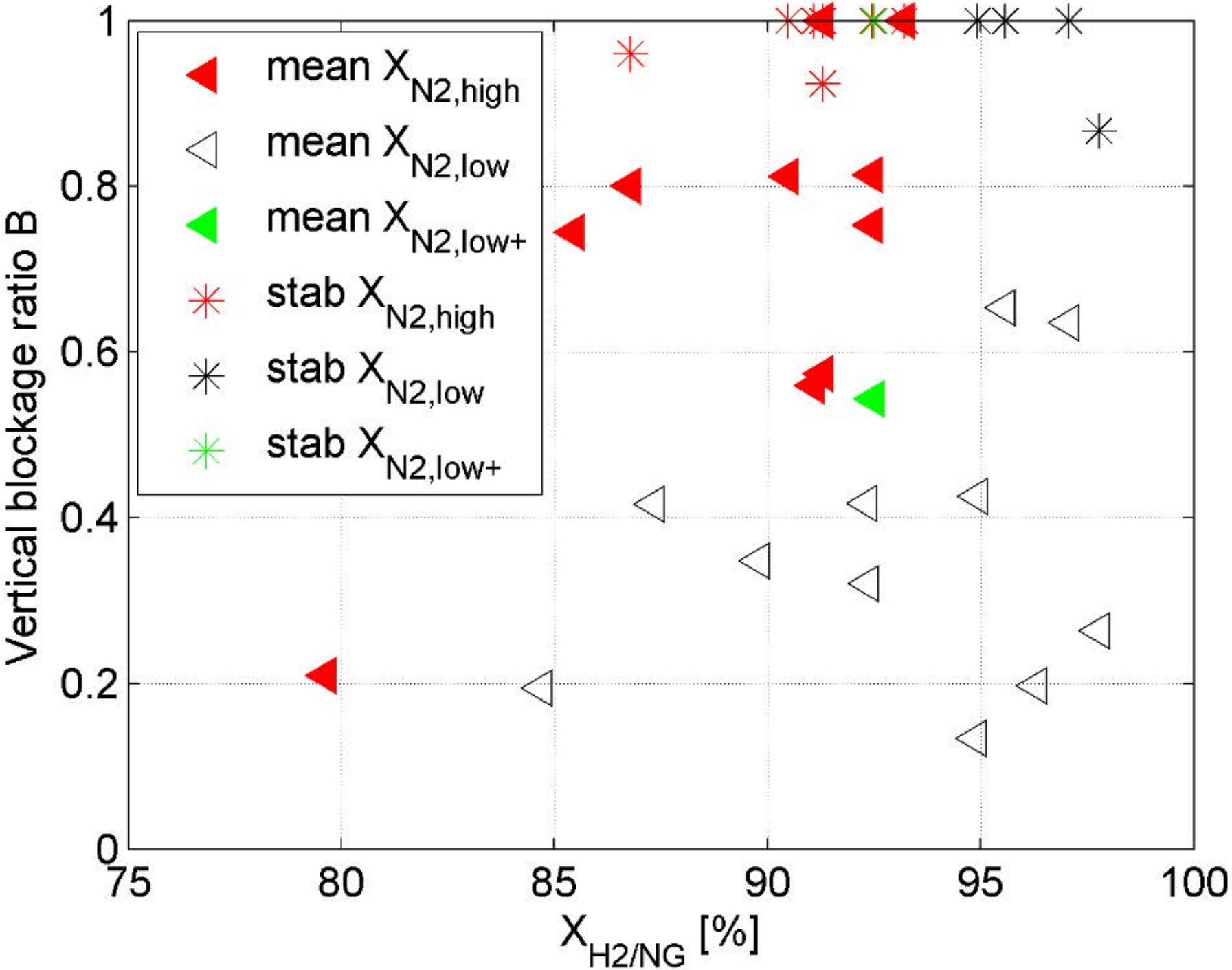
mean $X_{N2,high}$
mean $X_{N2,low}$
mean $X_{N2,low+}$
stab $X_{N2,high}$
stab $X_{N2,low}$
stab $X_{N2,low+}$
Vertical blockage ratio B
$X_{H2/NG}$ [%]
0
0.2
0.4
0.6
0.8
1
75
80
85
90
95
100